Astronomy & Astrophysics

XMM-Newton observations of the young open cluster Blanco 1[*,**]

I. X-ray spectroscopy and photometry

I. Pillitteri[1], G. Micela[2], S. Sciortino[2], F. Damiani[2], and F. R. Harnden Jr.[3]

[1] Dip. di Astronomia, Università di Palermo, Piazza del Parlamento 1, 90134 Palermo, Italy

[2] INAF – Osservatorio Astronomico di Palermo Piazza del Parlamento 1, 90134 Palermo, Italy
e-mail: giusi@astropa.unipa.it, sciorti@astropa.unipa.it, damiani@astropa.unipa.it

[3] Harvard-Smithsonian Center for Astrophysics, 60 Garden Street, Cambridge, MA 02138, UK
e-mail: frh@cfa.harvard.edu

Abstract. We present an X-ray study of the high metallicity young open cluster Blanco 1 based on *XMM-Newton* data. X-ray spectroscopy of cluster members is presented for the first time as well as new X-ray distribution functions of late-type stars. We detected all known dF and dG stars in the EPIC field and 80% and 90% of dK and dM stars, respectively. The X-ray spectral analysis of the X-ray brightest cluster stars and X-ray color analysis of a larger sample show that a model with two temperatures (at about 0.3 and 1 keV) explains the quiescent activity phase spectra.
We discuss also the nature of unidentified X-ray sources in the observed region and their X-ray spectral properties.

Key words. X-ray: stars – stars: activity – Galaxy: open clusters and associations: individual: Blanco 1

1. Introduction

Open clusters are powerful laboratories to test the models of star formation and evolution as well as the metal enrichment in the Galaxy. They are naturally selected samples of stars with the same age, composition and environmental formation conditions. In the last two decades, X-ray observations of open clusters have assumed greater importance. Since the early' 80s, the open cluster X-ray observations of first *Einstein* and subsequently ROSAT showed that young cluster stars are stronger X-ray sources than the Sun (see Micela 2002, and reference therein). The evolution of X-ray activity is correlated with the evolutionary angular momentum losses, older stars being less luminous than younger ones, but other, more subtle, factors like pre-main-sequence history and chemical composition could also play a role. The comparison of the properties of different clusters is essential for an understanding of the importance of these factors. It is expected that stellar chemical

composition influences the processes of coronal emission and activity: X-ray spectra of stars with high metal content are expected to have an enhanced line emission contribution with respect to low metallicity stars. Moreover, the extent of the convective zone in solar-type stars is also determined by metal content, thus resulting in a possible enhanced dynamo efficiency. Investigations of open clusters with different metallicity are of great importance for the study of the relation between stellar structure and X-ray activity.

Blanco 1 is a young open cluster noticeably more distant from the Galactic Plane (about 240 pc) than the young open cluster scale height (~100 pc). Its age, around 100 Myr, is very similar to that of the Pleiades and NGC 2516 clusters (de Epstein & Epstein 1985; Westerlund et al. 1988), while its metallicity ([Fe/H] = +0.23 dex) is significantly higher than that of the Sun and the Pleiades (Edvardsson et al. 1995; Panagi & O'Dell 1997; Jeffries & James 1999). The high metallicity of Blanco 1 offers a suitable benchmark for the connection between stellar structure, activity and convection. Measurements of Li abundance by Jeffries & James (1999) do not fit standard mixing models for stars of this age and metallicity, thus implying some Li-depletion inhibition. Our previous work (Micela et al. 1999a; Pillitteri et al. 2003, Paper I) based on ROSAT data showed that the cluster dG and dK stars have an overall X-ray emission similar to that of the Pleiades while the dM stars

in Blanco 1 appeared more luminous in the X-ray band with respect to the Pleiades and α Per clusters. Prior to Paper I, membership catalogues for stars down to late K types were based only on photometry (de Epstein & Epstein 1985; Panagi & O'Dell 1997), while a few radial velocity measurements were given in Jeffries & James (1999) and Edvardsson et al. (1995). In Paper I the membership of the cluster stars in the ROSAT field of view was defined by means of proper motion analysis and it was possible to derive X-ray luminosity distributions (XLDs) for dF, dG, dK and dM types. In that work, due to the limited sensitivity of ROSAT, the XLD of dM stars was significantly affected by the large number of upper limits. Furthermore, the lack of spectral capability of the ROSAT-HRI camera did not allow us to derive any spectral features of the cluster coronae. The *XMM-Newton* observation addresses these two issues: the large effective area of its three X-ray telescopes allows us to detect essentially all cluster members in the observed region and the moderate spectral resolution of the EPIC camera allows us to explore the main characteristics of the coronal spectra.

In this work we present the X-ray spectroscopy and photometric analysis of the cluster region as follows: in Sect. 2 we describe the observations, the basic processing of the data and the source detection results. In Sect. 3 we discuss the X-ray spectral analysis of the cluster stars and their XLDs. In Sect. 4 we discuss the nature of the unidentified sources and in Sect. 5 we summarize our conclusions.

2. Observation and data analysis

The observation studied here was performed with the *XMM-Newton* satellite in June 2002 during revolution 0461 with a nominal duration of 50 ks. The pointing, RA: $0^h02^m48^s$; Dec: $-30^d00^m00^s$ (J2000), was chosen to be the same as field 1 observed with the ROSAT HRI (Micela et al. 1999a). Because the $\sim30'$ field of view is slightly less than that of the ROSAT HRI ($\sim40'$), the optical catalog of Paper I is suitable for use here.

The *XMM-Newton* satellite is composed of three X-ray telescopes which observe simultaneously, accumulating photons in three CCD-based instruments: the twin MOS 1 and MOS 2 and the p–n (Turner et al. 2001; Strüder et al. 2001), all three detectors constituting the EPIC camera. Both of these imaging and non-dispersive instruments permit low resolution spectral analyses to be performed. Because a fraction of the flux collected with the two telescopes in front of the MOS CCDs is used to illuminate the dispersing grating array RGS, the MOS 1 and 2 collect fewer photons than does the p–n. The *Medium* filter was used for all three instruments during this observation. This filter was chosen to optimize the detector response in the soft band where it is known to be the bulk of the coronal X-ray spectrum, and, at the same time, to block optical photons (that could induce false X-ray events) of sources as bright as 8–10 m$_V$, which are expected to be observed in the field of view.

The preliminary processing of raw EPIC *Observation Data Files* data was done using the *epchain* and *emchain* tasks of the *SAS* version 5.3.3 software[1], which allow calibration

---

[1] See http://xmm.vilspa.esa.es/sas
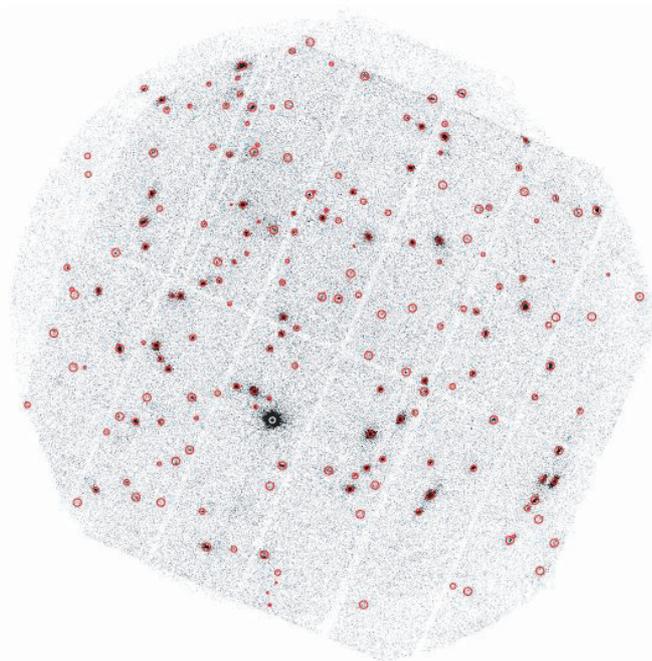
Fig. 1. Composite *p–n*, Mos 1 and Mos 2 X-ray image of the EPIC field; detected sources are indicated as circles with radii proportional to the wavelet detection scale.

both in energy and astrometry of the events registered in each CCD chip and to combine them in a single data file for MOS and *pn* detectors. We selected only events in the 0.3–5.0 keV band, with PATTERN ≤ 12 that marks only the events registered in up to four nearby pixels simultaneously. The energy upper bound reduces background contamination and improves source detection effectiveness. The background contribution is particularly relevant at high energies where coronal sources have very little flux and are often undetectable. Due to increased solar activity, however, XMM data are sometimes affected by an intense background level. This behaviour degrades the quality of the data, especially for investigations like ours that seek faint source detections, necessitating the use of time filtering. We have therefore selected time intervals by evaluation of a merit curve which maximizes the signal-to-noise ratio and retains only time intervals with low image count rates (cf. Sciortino et al. 2001). Only two narrow temporal segments, comprising ~750 s, were affected by a high count rate, leaving most of the observation time intact for analysis (screened fractions of total time were 48.6/49.4 and 51.0/51.7, for the *p–n* and the MOS 1 and 2, respectively). An exposure map for each EPIC instrument was created with the *SAS* task *eexpmap* in the same energy band as the selected events. The source detection has been performed on the sum of MOS and *p–n* datasets as described in the following, by means of the Wavelet Detection algorithm developed at the Osservatorio Astronomico of Palermo (Damiani et al. 1997a,b; Damiani et al., in preparation) adapted to the *XMM-Newton* EPIC case. The detection code has been modified in order to match the properties of the EPIC camera, taking into account the shape of the *Point Spread Function* (PSF) whose wings give a relevant contribution to the encircled

energy up to radii greater than 3 times the PSF core. The adopted PSF model follows the parameterization described in Ghizzardi (2001) and Saxon (2002), valid out to ~12′ off-axis. The code avoids the problem of spurious peaks in the convolved image due to sharp CCD edges by interpolating the image prior of convolution in the gaps and extrapolating beyond the boundaries with the nearest-to-local background. Following detection, count rates are obtained multiplying by the area of a reference instrument chosen by the user, as if the observation were carried out with that single instrument. We chose the MOS1 and calculated our count rate to flux conversion factor for the *Medium* filter used during our observation[2]. To choose detection thresholds, we performed a set of 100 simulations of empty fields with the same number of counts as in our observation. We then chose the threshold to retain at most only a single spurious source. After removal of several obvious spurious detections[3], 190 detected sources remained.

An optical catalog of 93 Blanco 1 members was derived in Paper I from GSC-II[4] data by means of proper motion and photometric selection to avoid any bias towards the X-ray properties of the sample. The analysis was also restricted to the field of view of ROSAT-HRI observations to maximize the effectiveness of selection. Forty of these 93 objects fell in the EPIC field of view. To this catalog we added the bright A-type star that lies in the EPIC field of view, assuming this star to be a member (Panagi & O'Dell 1997), notwithstanding its lack of proper-motion based membership.

While cross-identifying X-ray source and optical catalog positions, we found systematic offsets of 2.2″ and 0.4″ along RA and Dec, respectively, requiring that corrections be applied to the X-ray positions before definitive matches could be achieved. In this second iteration, we retained identifications for which the offset between X-ray and optical positions was ≤13″. This cross-identification radius represents a reasonable choice for minimizing the number of spurious identifications (whose expected number at 13″ is 0.86) while achieving the largest number of bona-fide identifications. We thus find 36 X-ray sources with optical cluster member counterparts and report their properties in Table 1. Exposure times and count rates listed in Table 1 are scaled to the reference instrument (MOS 1) that we chose for detection. For the five cluster stars that were not detected, we calculated upper limits the to count rate, flux and luminosity using the chosen detection threshold.

A search for optical counterparts of the remaining 154 X-ray sources, using the USNO-B1 (Monet et al. 2003), GSC-II and 2MASS[5] catalogs (Cutri et al. 2003) with a match radius of 13″ yielded a list of 90 counterparts in the visible

and infrared bands. We report the X-ray properties of these 90 sources in Table A.1, in which the last 3 columns show the number of matches in the three catalogs. Note that the USNO catalog yields an implausible number of matches for some sources, indicating problems with this catalog. In such cases, an extended object (e.g. a galaxy) can often be recognised in the finding chart.

After the identification process, 64 of 190 sources remained without counterparts. Due to the high galactic latitude of this pointing, we expect to have detected a small number of active field stars and a larger number of X-ray extragalactic sources (e.g., AGN galaxies or galaxy clusters). Properties of these unidentified X-ray sources will be discussed in Sect. 4.

3. Blanco 1 X-ray sources

3.1. X-ray spectral analysis

The spectral capabilities of the EPIC camera allow us to explore the coronal properties of cluster stars. We have used *p–n* data and XSPEC software to perform spectral analyses for six cluster stars (3 dK, 2dG and 1 late A) with more than 1000 X-ray counts, identifying relevant coronal temperature components and corresponding *emission measures* (EM). Spatial isolation of these sources minimized contamination by other sources. We then used the results of this analysis as a guideline for our subsequent analysis with X-ray color indices (see Sect. 3.2).

The star *ZS 76* underwent two flare-like episodes during the first half of our observation. This star is reported as binary in the catalog of Panagi & O'Dell (1997). Although the beginning of the first flare may not have been observed, the two flares appear to have durations of ~4 h. Here we present our analysis of the quiescent phase; the flare spectra will be analyzed in detail in a companion paper devoted to a study of the X-ray variability of the cluster. Stars *ZS46*, *ZS61* and *ZS75* exhibit no flares, although Kolmogorov-Smirnov tests indicate some type of variability at the 98%-confidence level; we will discuss these features in the context of our variability study. *ZS48* and *ZS54* do not show variability. Here we assume that the spectra of these five stars are representative of their normal, quiescent X-ray activity.

For our spectral analyses, we extracted events that triggered only one or two detector pixels at the same time (PATTERN ≤ 4), with energy in the 0.3–5.0 keV band and in a circular region within 35 or 40″ from the position of the sources depending on the spatial crowding. Spectra were binned to provide at least 25 counts per bin. In some cases for the background spectrum we chose an extraction region near but not centered on the source to avoid contamination from other X-ray sources. The redistribution matrix and response files were calculated at each source position. We fitted the data with a combination of two absorbed plasma thin emission models; a combination of 3 components did not improve the fits. To calculate the models and to fit the data, we used the APEC database, which contains the relevant atomic physics data for both continuum and line emission (Smith et al. 2001), driven by XSPEC software.

---

[2] In these data accumulated *p–n* events are ~3.2 times those recorded for each MOS detector.

[3] These were due to "hot pixels" not yet listed in calibration files at the time our work was done.

[4] The Guide Star Catalogue II is a joint project of the Space Telescope Science Institute and the INAF – Osservatorio Astronomico di Torino.

[5] 2MASS is a joint project of the University of Massachusetts and the Infrared Processing and Analysis Center/California Institute of Technology, funded by the National Aeronautics and Space Administration and the National Science Foundation.

Table 1. X-ray properties of Blanco 1 stars in the *XMM-Newton* – EPIC field. Identifiers from Panagi & O'Dell (1997) (ZS), from Micela et al. (1999a) (BLX). We named P stars those without an identifier from Paper I. Positions and $B - V$ color are taken from Paper I; exposure times and count rates are scaled to the MOS1 instrument; fluxes are calculated with a conversion factor of 5.69×10^{-12} erg cts^{-1} cm^{-2} (see Sect. 3.2).

Name	RA J2000	Dec J2000	Offset arcsec	Signif	$B - V$	Exp. time ks	Count rate cts. ks^{-1}	log flux erg s^{-1} cm^{-2}	log L_{X} erg s^{-1}	log $\frac{L_{\mathrm{X}}}{L_{\mathrm{bol}}}$
P1	0:01:37.8	−29:57:28.3	–	–	1.58	26.28	≤1.9	≤−14.15	≤28.72	≤−2.77
P2	0:01:52.6	−30:05:36.0	–	–	1.42	49.46	≤0.9	≤−14.27	≤28.60	≤−3.61
ZS37	0:01:53.4	−30:06:12.9	0.66	23.4	1.48	47.05	8.0 ± 0.6	−13.38	29.50	−2.49
ZS38	0:01:54.4	−30:07:42.0	2.11	39.25	1.04	44.98	16.9 ± 0.9	−13.06	29.82	−3.09
P3	0:01:54.5	−30:10:38.3	2.06	10.52	2.02	25.41	4.3 ± 0.7	−13.65	29.22	–
ZS40	0:01:56.9	−30:12:08.0	11.57	7.22	1.38	25.19	2.9 ± 0.5	−13.83	29.05	−3.31
ZS39	0:01:57.7	−30:09:28.8	2.11	7.84	0.1	30.11	2.3 ± 0.5	−13.92	28.96	−5.81
BLX7	0:02:00.8	−29:59:17.6	0.95	40.32	0.74	69.05	11.4 ± 0.6	−13.23	29.65	−3.79
BLX9	0:02:01.3	−29:57:55.3	1.14	13.57	1.5	67.89	2.0 ± 0.2	−13.97	28.90	−3.01
ZS43	0:02:03.7	−30:10:25.1	9.03	5.12	1.53	33.99	0.6 ± 0.2	−14.52	28.35	−3.44
ZS42	0:02:04.2	−30:10:34.5	3.64	19.66	1.35	32.62	6.9 ± 0.7	−13.44	29.43	−2.98
ZS45	0:02:18.5	−29:51:08.6	0.8	34.55	0.66	66.08	8.9 ± 0.5	−13.33	29.54	−4.10
ZS46	0:02:19.7	−29:56:07.6	0.66	64.35	1.17	94.38	14.3 ± 0.5	−13.13	29.75	−3.00
ZS48	0:02:21.6	−30:08:21.7	0.72	56.5	0.27	59.65	22.2 ± 0.9	−12.94	29.94	−4.50
P4	0:02:24.3	−30:06:02.9	–	–	1.40	84.87	≤0.4	≤−14.58	≤28.29	≤−3.98
ZS53	0:02:24.3	−30:09:09.0	1.38	27.95	1.53	63.4	5.1 ± 0.4	−13.57	29.30	−2.51
BLX17	0:02:25.9	−29:52:39.2	2.05	39.11	1.42	82.75	7.2 ± 0.4	−13.43	29.45	−2.77
ZS54	0:02:28.2	−30:04:43.6	0.22	57.26	0.94	97.82	11.9 ± 0.5	−13.21	29.67	−3.39
ZS61	0:02:34.8	−30:05:25.6	0.83	79.74	0.84	102.3	18.2 ± 0.6	−13.02	29.85	−3.38
ZS62	0:02:35.4	−30:07:02.0	2.13	31.12	0.63	71.92	6.1 ± 0.4	−13.5	29.38	−4.34
BLX24	0:02:48.4	−29:53:53.8	4.33	23.53	1.58	75.28	4.0 ± 0.4	−13.68	29.20	−2.31
BLX26	0:02:51.5	−29:54:49.4	2.04	19.11	1.52	105.96	1.6 ± 0.2	−14.07	28.8	−3.04
P5	0:02:52.2	−29:47:00.9	3.2	10.66	1.47	44.29	2.1.0 ± 0.3	−13.95	28.92	−3.10
BLX27	0:02:54.2	−30:06:55.9	0.7	23	1.42	95.04	3.6 ± 0.3	−13.72	29.15	−3.07
ZS77[a]	0:02:55.1	−30:08:53.8	–	–	0.03	58.1	≤ 0.6	≤−14.44	≤28.43	≤−6.55
ZS76[b]	0:02:56.4	−30:04:45.1	0.24	226.64	0.76	113.81	110.3 ± 1.3	−12.24 (−12.68)	30.63 (30.19)	−2.76 (−3.20)
ZS75	0:03:00.3	−30:03:21.8	0.26	65.99	0.79	121.93	12.0 ± 0.4	−13.21	29.67	−3.67
ZS71	0:03:02.9	−29:47:44.2	0.25	47.78	1.37	58.22	20.4 ± 0.8	−12.97	29.90	−2.48
ZS84	0:03:10.8	−30:10:49.1	1.64	35.03	0.52	58.35	11.8 ± 0.6	−13.21	29.66	−4.32
BLX37	0:03:11.5	−29:58:10.2	1.33	22.75	1.51	102.68	2.7 ± 0.2	−13.85	29.02	−2.87
ZS95	0:03:16.5	−29:58:47.7	1.46	33.16	0.75	109.05	4.6 ± 0.3	−13.62	29.25	−4.17
ZS91	0:03:20.6	−29:49:22.9	0.92	25.72	0.44	57.84	6.5 ± 0.5	−13.47	29.40	−4.73
P6	0:03:20.8	−29:51:52.8	–	–	1.36	71.62	≤0.6	≤−14.43	≤28.45	≤−3.95
ZS96	0:03:21.8	−30:01:10.8	0.54	45	0.25	95.73	8.2 ± 0.4	−13.37	29.50	−4.99
P7	0:03:22.5	−29:51:52.8	2.57	11.52	1.45	69.89	2.0 ± 0.3	−13.98	28.9	−3.21
ZS94	0:03:24.2	−29:56:23.1	2.22	22.3	1.39	79.39	3.5 ± 0.3	−13.74	29.13	−3.19
ZS90	0:03:24.4	−29:48:49.6	0.72	20.09	0.33	11.56	14.0 ± 1.7	−13.14	29.74	−4.61
ZS93	0:03:24.7	−29:55:14.8	0.75	32.3	0.93	79.72	7.1 ± 0.4	−13.43	29.44	−3.63
BLX46	0:03:34.5	−29:58:30.5	0.9	26.42	1.56	75.84	4.4 ± 0.3	−13.64	29.24	−2.28
P8	0:03:39.9	−29:58:45.0	2.34	5.45	1.45	69.21	0.8 ± 0.2	−14.38	28.49	−3.62
ZS107	0:03:50.2	−30:03:55.9	4.45	7.46	1.15	21.55	2.4 ± 0.5	−13.9	28.97	−3.80

[a] Star added from Panagi & O'Dell (1997) catalog, see text.
[b] In parentheses flux, log L_{X} and log $L_{\mathrm{X}}/L_{\mathrm{Lbol}}$ of quiescent phase.

Table 2. Best fit parameters derived from the spectral analysis of six cluster brightest X-ray sources. The spectral types are estimated from $B - V$ assuming Main-Sequence stars (see Lang 1992). The error ranges refer to $\pm 1\sigma$ level.

Name	Sp. type	T_1 (keV)	T_2 (keV)	$Z/Z_\odot$	$\log EM_1$ (cm^{-3})	$\log EM_2$ (cm^{-3})	χ^2_ν (d.o.f.)	$P(\chi > \chi_0)$
$ZS\,46$	K5	$0.32^{+0.02}_{-0.03}$	$1.04^{+0.04}_{-0.07}$	$0.23^{+0.08}_{-0.05}$	$52.58^{+0.09}_{-0.10}$	$52.52^{+0.08}_{-0.08}$	1.16 (34)	23.5%
$ZS\,48^a$	A8	$0.60^{+0.02}_{-0.02}$	–	$0.9^{+0.1}_{-0.2}$	$52.61^{+0.09}_{-0.1}$	–	1.48 (26)	5.6%
$ZS\,54$	K2	$0.40^{+0.03}_{-0.05}$	$0.90^{+0.16}_{-0.04}$	$0.21^{+0.08}_{-0.05}$	$52.54^{+0.12}_{-0.07}$	$52.44^{+0.14}_{-0.11}$	1.25 (31)	15.7%
$ZS\,61$	K0	$0.33^{+0.02}_{-0.04}$	$1.06^{+0.07}_{-0.09}$	$0.22^{+0.06}_{-0.05}$	$52.72^{+0.04}_{-0.09}$	$52.57^{+0.08}_{-0.08}$	0.78 (46)	85.1%
$ZS\,75$	G8	$0.29^{+0.03}_{-0.02}$	$1.02^{+0.09}_{-0.08}$	$0.17^{+0.07}_{-0.04}$	$52.63^{+0.09}_{-0.10}$	$52.52^{+0.07}_{-0.08}$	1.02 (34)	43.6%
$ZS\,76^b$	G8	$0.35^{+0.05}_{-0.03}$	$0.99^{+0.04}_{-0.04}$	$0.22^{+0.05}_{-0.05}$	$53.03^{+0.09}_{-0.32}$	$53.12^{+0.03}_{-0.12}$	0.82 (72)	87.8%

[a]: For ZS48 the model is 1-T VAPEC, $Z/Z_\odot$ refers to Fe abundance, O abundance is $0.4^{+0.2}_{-0.02}$.

[b]: For $ZS\,76$ we report the quiescent spectrum parameters.

In all cases we found $N_{\mathrm{H}} \sim 3 \times 10^{20}$ cm^{-2} to be consistent with A$_V$ from photometry estimates (Epstein 1968; de Epstein & Epstein 1985; Westerlund et al. 1988) and therefore fixed it at this value. Abundances were scaled on the solar values of Anders & Grevesse (1989), leaving as free parameters the temperatures, a global abundance value and the emission measures (EM) of the two thermal components. Our best-fit parameters are reported in Table 2 and the corresponding spectra are shown in Fig. 2. For late-type stars (i.e. $ZS\,46, ZS\,54, ZS\,61, ZS\,75, ZS\,76$) the 2-T model describes the shape of the coronal spectrum quite well and indicates main temperature components around 0.3 and 1.0 keV. The ratio of emission measures EM_2/EM_1 is in the 0.7–1.2 range. The global coronal abundance parameter, determined mostly by the Fe line complex around 1 keV, is always significantly lower than the solar value. Similar results for the temperature value, emission measure ratio and coronal abundances were found by Briggs & Pye (2003) in an analogous spectral analysis of Pleiades solar-type stars observed with *XMM-Newton*. Gagné et al. (1995) previously found a 2-T model to be required to explain ROSAT PSPC spectra of Pleiades solar-type stars, although emission measure ratios found in that work were greater than 1, possibly indicating a more significant hot component. The need for lower than solar coronal abundances in the Blanco 1 coronae could imply that photospheric composition does not constrain spectral features of the coronal plasmas, but fitted emission measures are related to the metallicity values derived in this global fitting analysis, thus preventing a definitive abundance study. For the Pleiades stars HII 1032, 1100, 1348 and 1516 studied by Briggs & Pye (cf. their Table 3) with a 2-T analysis in the same spectral range, the mean EMs of hot and cool components are on average ~0.3 dex lower than those of our sample. By also including HII 1110 and 1280, two dK late stars with less than 500 X-ray counts, we found a more marked difference. However, we discarded these stars in the comparison because of their poor statistics. A comparison of our L_{X} values for Blanco 1 with those for the Pleiades observations indicates that different parts of the XLDs are being sampled in the two cases: we are modeling sources in the high activity tail ($\log L_{\mathrm{X}} \sim 29.7$) while Briggs & Pye studied

stars over a wider range of luminosity. This likely explains the differences noted above.

The spectrum of the A8 star $ZS\,48$ differs from that of solar type stars, and is well fit with a 1-T model with $kT \sim 0.6$ keV[6]. We allowed abundances of Fe and O to vary (see caption of Table 2) and kept all other metallicities fixed at the solar value. Stellar structure models predict that an A8 star with Blanco 1 metallicity would have a very shallow convective zone (Siess et al. 2000) and hence would exhibit very little X-ray emission. In the case of a binary system unresolved in X rays, emission is often assigned to the late companion. Because this star is flagged as a possible binary in the Guide Star Catalog II[7], a late companion could be responsible for the X-ray spectrum. If this were the case, however, its spectrum should resemble those of other late type stars. We therefore suggest instead that the emission is intrinsic.

3.2. X-ray colors, fluxes and luminosities.

Although the spectra of most cluster members have relatively poor statistics, we can characterize their coronal emission by means of *X-ray colors indices* and a grid of optically-thin coronal plasma models; a similar analysis method was employed by Damiani et al. (2003) on *Chandra* ACIS-I data. We chose three bands in which to accumulate EPIC source photons from the *p–n* detector (*soft*: 0.3–0.75 keV; *medium*: 0.75–1.5 keV and *hard*: 1.5–5.0 keV) and calculated *colors* as follows:

$$CR1 = 2.5 \log \frac{N_{\mathrm{medium}}}{N_{\mathrm{soft}}}$$

$$CR2 = 2.5 \log \frac{N_{\mathrm{hard}}}{N_{\mathrm{medium}}}.$$

These bands were chosen to minimize errors in each band. Source photons were extracted from circular regions of 20″ radius, and the background was obtained from annuli with radii

---

[6] Note however that the EPIC *p–n* bandpass is rather insensitive to any cool component below 0.3 keV.

[7] Available through the Vizier web database: http://vizier.u-strasbg.fr
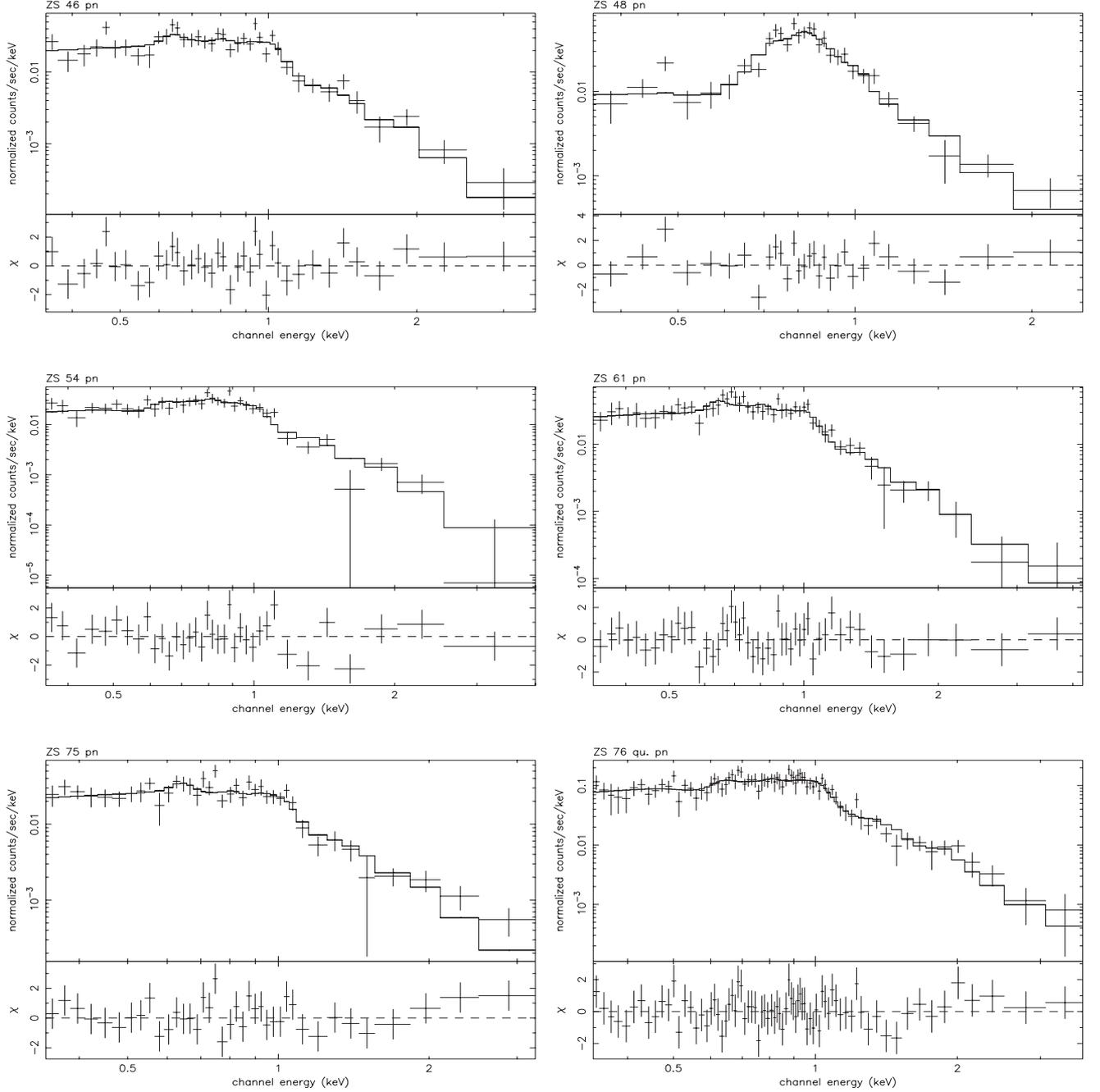
Fig. 2. X-ray spectra of the Blanco 1 brightest X-ray sources.

of 22.5″ and 30″. Smaller extraction radii than for detection are needed here to minimize contamination from nearby sources, especially in the case of the faint sources. Differences of encircled energy at the chosen radii between soft, medium and hard bands are negligible (≤2%) and were therefore ignored.

We computed a grid of models with XSPEC, adopting a 2-T APEC model with photoelectric absorption. To reduce the number of parameters we used the above X-ray spectroscopy results as a guideline, fixing the absorption N_H at 3×10^{20} cm^{-2}, the lower temperature at 0.33 keV and the abundances $Z = 0.25\ Z_\odot$ (the median of values obtained in the detailed spectral fits); this left high temperature, in the range 0.6–5.0 keV, and the *EM* ratio of the two APEC components (range 0.2–20)
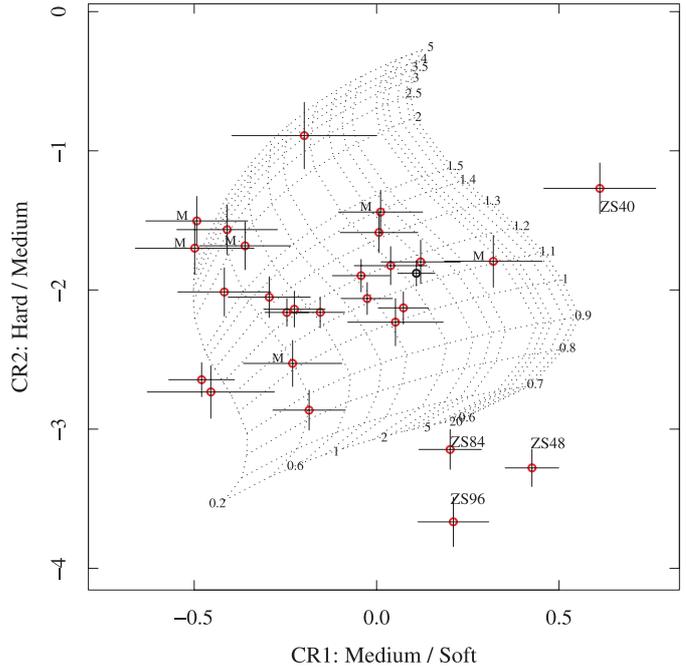
as the only two free parameters. We then calculated the expected *CR*1 and *CR*2 colors over a grid of 240 spectra. Table 3 reports the observed *CR*1 and *CR*2, while Fig. 3 shows the corresponding points in the *CR*1 − *CR*2 plane. All cluster sources have *CR*2 color indices below zero, while the *CR*1 index spans values around zero. Most of the cluster sources are included in the region explored by the model grid and broad agreement is found for the stars analyzed in detail in Sect. 3.1. Star *ZS48* lies outside the grid, as expected because its spectrum was adequately fitted with a 1-T model at 0.6 keV. Analogously, the position of *ZS96* in the diagram suggests that a 2-T model is not required to describe this A-type star. Apparently discrepant CR values of the G star *ZS84* are probably due to the presence

Table 3. X-ray colors $CR1$ and $CR2$ in the bands: 0.3–0.75, 0.75–1.5, 1.5–5.0 keV defined in Sect. 3.2 for the sample inside the grid of Fig. 3. The last column reports the count to flux conversion factor in units of 10^{-12} erg cts^{-1}cm^{-2}.

Name	$CR1$	$CR2$	CF
BLX24	−0.49	−1.5	5.64
BLX27	−0.41	−1.57	5.81
BLX9	−0.5	−1.7	5.64
BLX46	−0.23	−2.53	5.32
ZS53	−0.36	−1.68	5.7
ZS94	−0.42	−2.01	5.49
ZS93	−0.29	−2.05	5.61
ZS61	−0.25	−2.16	5.57
ZS71	−0.23	−2.14	5.57
ZS75	−0.15	−2.16	5.57
ZS54	−0.03	−2.06	5.76
ZS95	−0.48	−2.64	5.14
ZS62	−0.18	−2.86	5.22
ZS39	−0.2	−0.89	7.12
BLX37	0.01	−1.44	6.3
BLX17	0.01	−1.59	6.22
ZS76	0.32	−1.79	6.65
BLX7	0.04	−1.83	6.13
ZS38	−0.04	−1.9	6.13
ZS45	0.12	−1.8	5.82
ZS37	0.32	−1.79	6.33
ZS46	0.07	−2.13	5.69
ZS42	0.05	−2.23	5.69

Fig. 3. $CR2$ vs. $CR1$ scatter plot for the cluster X-ray sources based on *p–n* data. The region explored by the model grid is traced; values of EM_2/EM_1 are indicated at the bottom of the grid, and high temperature component values (units: keV) are indicated at the right edge. "M" denotes dM type stars, while stars outside the grid and discussed in the text are labelled with identifiers.

of a nearby object, as suggested by an inspection of the optical finding chart. Note too that the far-off axis position of *ZS40* and the low statistical precision of its spectrum have probably invalidated its CR estimates. In summary, a significant fraction of the sample is found to have a hot temperature component between 0.8 and 1.5 keV, with weights generally lower than (or at most equal to) the cool component. Some M type stars are also found at higher temperature ($\sim$1.5–5 keV, see Fig. 3). The agreement of this CR method with the spectral analysis suggests that the CRs offer a good description of the coronal spectra in terms of 2-T models.

By evaluating the flux obtained from the best–fit spectral models we derived a conversion factor CF between count rate and flux (cf. Table 3). The median value is 5.69×10^{-12} erg cts^{-1} cm^{-2}, with a 1-σ range of 5.52–6.25×10^{-12} erg cts^{-1} cm^{-2} corresponding to uncertainties of -3% and $+10\%$, respectively. We calculated X-ray fluxes and luminosities in the 0.3–5.0 keV band (cf. Table 1) assuming a

distance of 250 pc (Panagi & O'Dell 1997; Westerlund et al. 1988; de Epstein & Epstein 1985) as in previous works. Note however that the cluster distance derived from the *Hipparcos* satellite is 262 pc (Robichon et al. 1999), which would lead to a difference of $\sim$+0.02 in log L_X. Table 1 gives count rates, fluxes and luminosities of the cluster sample. Count rate errors calculated by the detection code have a median value of $\sim$7% (4% and 19% at the 0.1 and 0.9 quantiles of distribution, respectively).

In Fig. 4 we plot Blanco 1 log L_X vs. $(B - V)_0$ and for comparison, median and 0.1–0.9 quantiles of log L_X for the Pleiades (Micela et al. 1999b, 1996). The new data permit us to detect 11 X-ray faint members for which only upper limits were obtained with ROSAT, giving an XMM detection percentage of 88% vs. 61% for ROSAT.

Three A-type stars of the Paper I catalog are detected, but *ZS 77* (the star added from Panagi's list) is not and instead we estimate its upper limit. All dF and dG type stars in the EPIC field of view (numbering 3 and 6, respectively) were detected, and the dK and dM type detection fractions were 15/18 and 9/10 (83% and 90%), respectively.

Figure 4 suggests a rise of X-ray luminosities at $(B - V)_0 \sim 0.1$ possibly indicating the onset of convection. The dynamo mechanism responsible for coronal emission may start at these spectral types, corresponding to stars with masses $\sim$2 $M_\odot$. For comparison, ROSAT nearby star data (Schmitt 1997) show detections at similar types ($B - V \sim 0.2$). X-ray luminosities have a spread of $\sim$0.5–0.7 dex in dF, dG and early dK types. Furthermore, a drop of about 1 dex in log L_X is visible in late
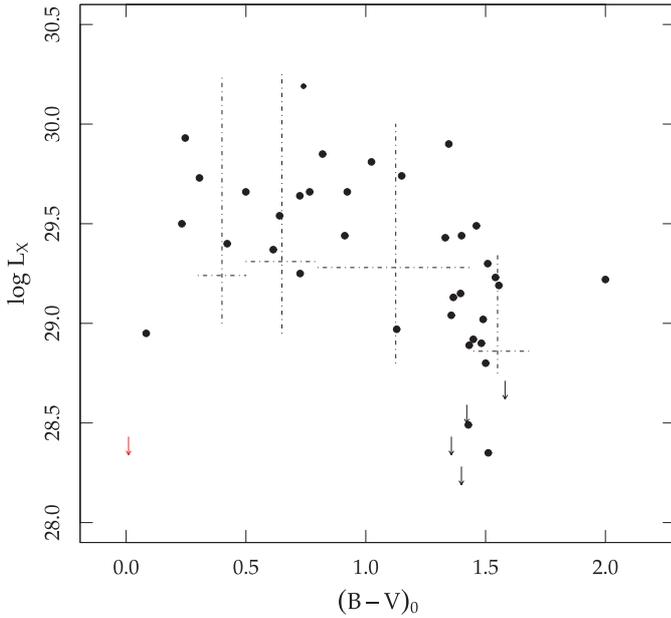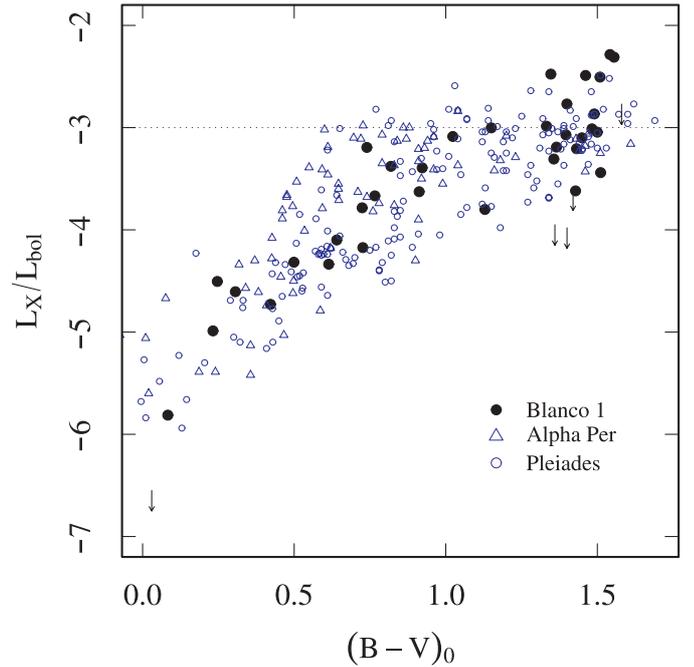
Fig. 4. $\log L_X$ vs. $(B - V)_0$ scatter plot for the Blanco 1 X-ray sources. Horizontal lines are medians of $\log L_X$ for the Pleiades, while vertical lines are the 0.1–0.9 quantiles of Pleiades data in each spectral type.
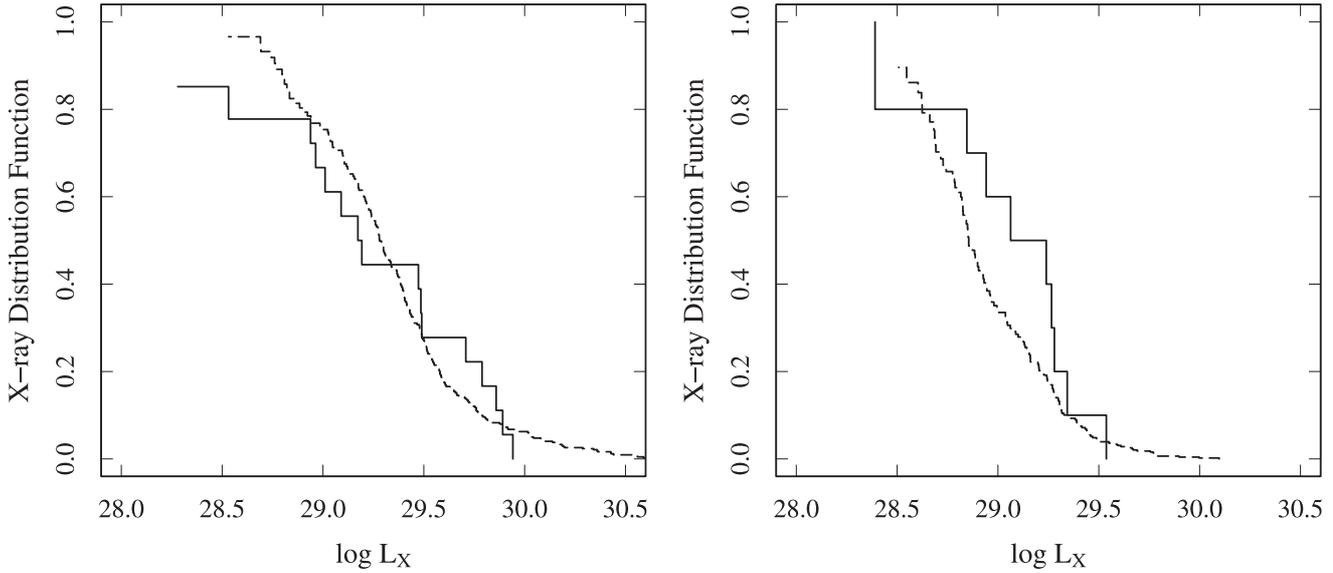

Fig. 5. Ratio $\log L_X/L_{bol}$ versus $(B - V)_0$ for Blanco 1 cluster stars. ROSAT data (detections only) of other clusters are shown with triangles for α Per (Randich et al. 1996), and with circles for the Pleiades (Micela et al. 1999b; Stauffer et al. 1994). These data have been retrieved from the WEBDA database: `http://obswww.unige.ch/webda`

dK and dM stars with the lowest detected source having a flux of $\log f_X = -14.52$ corresponding to $\log L_X = 28.35$.

It is known that young, active stars exhibit a saturation of the ratio $\log L_X/L_{bol}$ around the value -3 but it is not yet clear whether the saturation is due to the filling of the stellar surface with active coronal regions or to an intrinsic self-limiting mechanism in the dynamo. The dependence of X-ray activity on age is thought to be due to the relation between age and angular momentum losses: younger stars rotate more rapidly and as a consequence have more active X-ray coronae (Pizzolato et al. 2003, and references therein). Jardine (2004) and Jardine & Unruh (1999), through modelling of coronae at high rotation rates, have suggested that centrifugal force can limit the size of coronal loops in fast rotators, thus explaining the saturation phenomenon. Studies of open clusters and star formation regions have shown that the onset of saturation in stars with ages of a few hundred million to a billion years is observed as follows: for stars with $(B - V)_0 \sim 0.6$–0.7, saturation sets in at ages of a few Myr up to 100 Myr (IC 2391/IC 2602, α Per and Pleiades) for $(B - V)_0 \sim 1$, at 300 Myr (NGC 6475); and for $(B-V)_0 \sim 1.4$, at 600 Myr (Hyades, Praesepe) (Randich 1997). This pattern agrees with the rotation slow-down – X-ray activity decrease for stars of greater and greater ages. For Blanco 1, we have calculated stellar $\log L_X/L_{bol}$ ratios with L_{bol} values by interpolating on $(B - V)_0$ from a 100 Myr, $Z = 0.03$ isochrone model (Siess et al. 2000) (see Table 1)[8]. As seen in Fig. 5, the large scatter in Blanco 1 dM stars with $\log L_X/L_{bol} \geq -2.5$ obscures any evidence of saturation in these late-type stars. However, nearly all of these objects underwent a flare-like event during our observation, causing them to appear at higher $\log L_X/L_{bol}$ values than the remaining sample. Without these

objects the distribution of $\log L_X/L_{bol}$ appears to flatten around $(B - V)_0 = 1$, equivalent to 0.8 $M_\odot$. Interpreted in this manner, the L_X/L_{bol} ratios for Blanco 1 are consistent with those of other coeval clusters.

The Kaplan-Meier estimators of $\log L_X$ cumulative distribution functions for the censored data of dK and dM stars are shown in Fig. 6. For comparison we report also the analogous Pleiades distributions from ROSAT data (dashed line). These XLDs suggest a probable difference in the case of dM stars, as already reported in Paper I. We observe that the XLD of dM stars in Pleiades and Blanco 1 overlap at high L_X for values down to $\sim$29.4, then the dM stars of Blanco 1 appear more luminous, with a median of $\sim$29.2 while Pleiades stars exhibit a median of $\sim$28.8. A *Wilcoxon* two-sample test applied to the dM data of Blanco 1 and the Pleiades show that the two distributions differ at a confidence level of 97%, while a *Gehan* test yields a difference at only the 94% level (see Feigelson & Nelson 1985 for a discussion of the Kaplan-Meier estimator and two sample tests we used here). If the difference is true, this could arise by the enhanced metallicity of Blanco 1 stars with respect to the Pleiades ([Fe/H] = +0.23, Edvardsson et al. 1995). The higher metallicity is expected to enhance the radiative losses, due to line emission, which dominates the coronal spectra at temperatures of $\sim$0.3$-$1 keV, such as those found in our spectral analysis.

The dK stars of Blanco 1 have an emission level similar to that of the Pleiades, confirming the result already presented in Paper I. As for dM stars, the dK XLD is well determined, with upper limits occurring only in the lower tail.

---

[8] For one star, *P3*, no ratio is given because extrapolation to such a large $B - V$ value was considered unreliable.

Fig. 6. Kaplan-Meier estimator (solid line) of cumulative distribution functions (XLD) of log L_X of dK (*top panel*) and dM stars (*bottom panel*). Dashed lines show analogous ROSAT data for the Pleiades (Micela et al. 1999b, 1996); comparison with these data are discussed in the text.
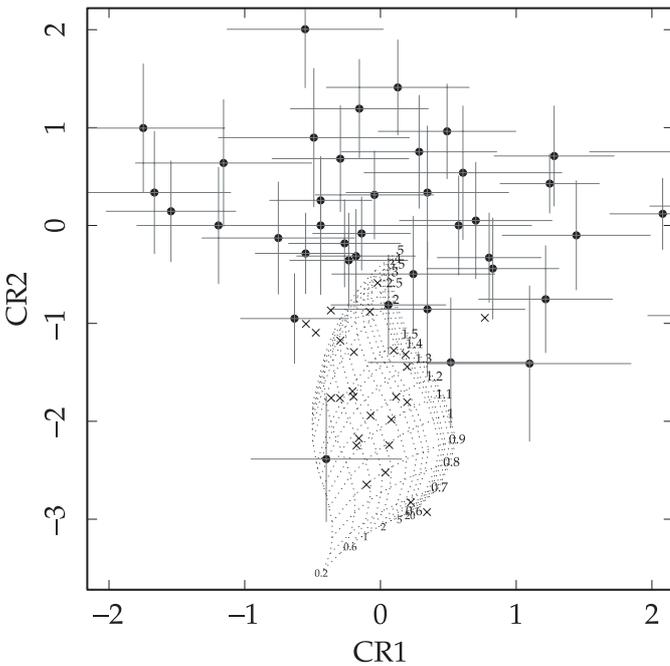

Fig. 7. X-ray color diagram of the unidentified sources. For comparison, Blanco 1 source data (crosses) and the model grid described in Sect. 3.2 are also shown.

For high-metal content dK stars (Pizzolato et al. 2001), models predict higher emission levels than for low metallicity dK stars, but we do not see this in our data. Other factors, such as a different distribution of rotational velocities, might explain this apparent shortcoming of the models.

4. Other X-ray sources and the completeness of cluster sequence

The detection process revealed 64 X-ray sources with no known counterpart in the optical and infrared bands. In Table B.1 we give their positions, offsets, count rates and
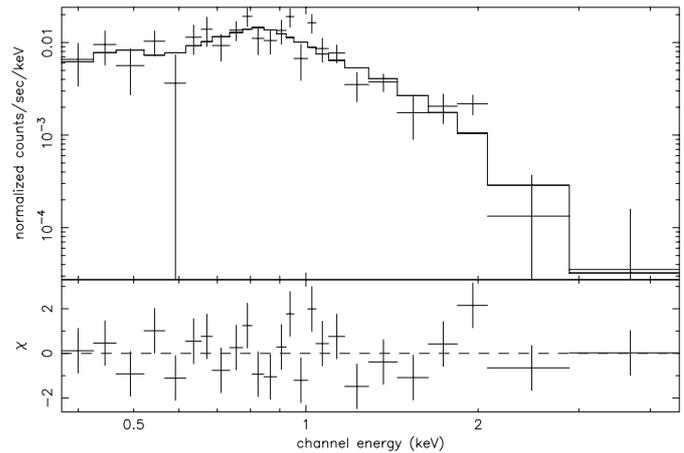
Fig. 8. X-ray spectrum of the low mass flaring star No. 26 in Table A.1.

detection significance. We have calculated the X-ray colors for the brightest sources as described above. The color–color diagram in Fig. 7 reveals that most of these objects appear in a different region, well separated from cluster member sources, and implies they have different spectra. Most of these sources are expected to be extragalactic because of the high latitude of this observation. Unidentified sources Nos. 16 and 23 of Table B.1 do have X-ray colors within the model grid region, suggesting that their spectra are similar to those of cluster coronae. These two objects may be unknown cluster stars with very low mass but high X-ray activity. The positions of sources Nos. 39 and 51 fall within $10''$ of two X-ray sources (BLX 35 and BLX 40) previously reported in Table 4 of Micela et al. (1999a).

We focused our attention on two of the sources with optical counterparts not belonging to Blanco 1: the flaring X-ray source No. 26 and the star BLX 16 (respectively Nos. 26 and 169 in Table A.1). In the proper motion analysis in Paper I, the optical counterpart of the source No. 26 had a low probability of cluster membership, and its photometry, consistent

with the low mass part of the cluster main sequence, suggests that this is a X-ray active, low mass field star. The X-ray light curve exhibits a ~20 ks flare at the beginning of the observation. Its spectral analysis (see Fig. 8) favors an absorbed 1-T model with a temperature around 0.65 keV and a N_H value of ~1.6×10^{21} cm^{-2}. The abundance parameter is driven to a very low value (0.03 $Z_\odot$) to obtain a good fit. Its position in the X-ray color diagram (outside the region explored by the 2-T models) also suggests a different spectrum.

BLX 16 (No. 169 in Table A.1) is an X-ray active source reported in Micela et al. (1999a) with properties similar to those of the lowest mass stars of the cluster. In Paper I we discarded it as a cluster member because its position in the color magnitude diagram was slightly off the cluster main sequence. We were able to assign a M1Ve spectral type from its spectrum obtained in an optical follow-up, however, and with the present X-ray color data, we find its spectrum in agreement with that of the other cluster stars. We therefore cannot rule out the possibility of this star being another low mass member of the cluster. If accepted as a cluster member, its flux would be $\log f_X = -13.75$ erg s^{-1} cm^{-2}, and its X-ray luminosity would be $\log L_X = 29.13$, consistent with the L_X XLD of dM stars in Fig. 6.

5. Summary

We have presented our analysis of an *XMM-Newton* observation of the young open cluster Blanco 1 addressing the issues of the completeness of detection among X-ray cluster sources and, for the first time, of low resolution X-ray spectroscopy of its members.

We have detected 190 X-ray sources by using a wavelet-based algorithm developed specifically for the EPIC camera. Detections were derived from the combined MOS 1, 2 and *p–n* datasets, making full use of the EPIC camera capability and improving the detection sensitivity. Of the 190 detected sources, 36 are identified with cluster members, while 5 cluster members remain undetected. Compared with previous ROSAT

observations, the *XMM-Newton* rate of detection has increased from 61% to 88%.

Six cluster sources with more than 1000 counts were then used for spectral analysis. A 2-T model fits the main spectrum features well and allows us to identify a "cool" component around 0.3 keV and a "hot" component around 1 keV, both with similar emission measures. These values are in good agreement with the XMM description of coronal spectra for young active stars like the Pleiades.

A 1-T model at ~0.6 keV explains the soft spectrum of an intermediate type star (spectral type ~A8) of the cluster. We consider that the X-ray emission is intrinsic to the A star itself and not due to an unresolved late companion.

By means of two X-ray color indices, the X-ray spectral properties of a larger cluster sample were explored and found to be consistent with the above 2-T model.

The X-ray luminosity distribution function of dM-type stars of the cluster indicates a probable difference in emission levels with respect to the Pleiades. Saturation of $\log L_X/L_{bol}$ is not clearly evident down to mid-K stars, slightly later than in the Pleiades.

Appendix A lists non-cluster optical counterparts for 90 of the 190 X-ray sources, identified either with the GSC-II and USNO-B1 optical catalogs or with the 2MASS infrared catalog. One star is suggested as a new probable low-mass cluster member.

64 sources are listed in Appendix B that remain unidentified: most of them show X-ray colors quite different from those of the cluster, suggesting a different nature. However, for two of them the color analysis in Sect. 4 suggests agreement of their spectrum with those of cluster coronae.

Appendix A: X-ray sources with optical counterparts in the GSC2, USNO-B1 and 2MASS catalogs

Table A.1. List of X sources with a counterpart in the optical and infrared catalogs USNO, GSC2 and 2MASS. The exposure times and the count rates are scaled on the MOS1 instrument. The final columns report the number of positional matches within 13″ in these catalogs.

No. Src X	RA (J2000)	Dec (J2000)	Pos. Err. arcsec	Exp. time ks	Rate cts/ks	No. opt. id. USNO	No. opt. id. GSC2	No. opt. id. 2MASS
2	00:02:36.2	−30:13:37.6	5.6	37.8	1.7 ± 0.4	3	1	0
3	00:02:57.3	−30:13:3.1	1.7	51.03	0.4 ± 0.1	1	0	0
4	00:02:13.2	−30:12:58.9	5.3	26.61	2.7 ± 0.5	1	0	0
5	00:02:16.5	−30:12:43.7	4.5	28.21	1.2 ± 0.3	1	0	0
9	00:02:58	−30:11:12.9	3.5	61.64	4.3 ± 0.4	1	0	0
10	00:03:4.7	−30:10:57.5	3.8	61.89	1 ± 0.2	8	1	0
21	00:03:20.7	−30:08:42.5	5.5	65.21	1 ± 0.2	11	1	1
22	00:01:58.5	−30:08:36	3.3	45.96	7.8 ± 0.6	2	0	0
25	00:03:35.1	−30:08:5.5	2.4	43.52	6.1 ± 0.5	1	0	0
26	00:02:39.2	−30:08:4.7	1.7	82.71	11.1 ± 0.5	1	1	1
27	00:02:56.8	−30:07:55.6	5.5	86.01	0.8 ± 0.2	2	0	0

Table A.1. continued.

No. Src X	RA (J2000)	Dec (J2000)	Pos. Err. arcsec	Exp. time ks	Rate cts/ks	No. opt. id. USNO	No. opt. id. GSC2	No. opt. id. 2MASS
28	00:02:33.6	−30:07:53.5	5.1	80.64	1 ± 0.2	4	1	1
29	00:03:28.3	−30:07:44.7	3.4	62.66	1.4 ± 0.2	1	0	1
31	00:01:56.8	−30:07:35.1	2.2	47.28	8 ± 0.6	1	1	0
32	00:02:38	−30:07:26.7	3.5	87.42	1 ± 0.2	1	0	0
34	00:02:11.9	−30:07:4.2	2.3	65.41	4.3 ± 0.4	1	0	0
38	00:02:21.4	−30:06:48	3	72.7	1.8 ± 0.2	1	0	0
40	00:02:32	−30:06:38.5	2.5	86.98	2.5 ± 0.2	1	0	0
42	00:03:14.4	−30:06:11.6	4.3	82	1.6 ± 0.2	1	0	0
44	00:03:32.6	−30:05:19.8	4.1	66.68	0.7 ± 0.2	2	0	0
45	00:03:20.7	−30:04:50.4	2.8	85.39	1.7 ± 0.2	1	1	1
48	00:02:07.6	−30:04:44.4	3.5	58.64	4.5 ± 0.4	2	2	2
50	00:03:12.9	−30:04:40.3	2.4	97.1	0.7 ± 0.1	1	0	1
51	00:03:29.8	−30:04:34.8	4.8	74.11	1.4 ± 0.2	1	1	1
52	00:02:24.8	−30:04:24.1	3.4	64.25	1.2 ± 0.2	1	1	1
53	00:01:48.6	−30:04:18.8	3.4	48.17	1.8 ± 0.3	1	0	0
54	00:02:59.9	−30:04:7.6	2.6	116.78	0.6 ± 0.1	2	0	0
56	00:02:56.9	−30:03:43.6	2.2	122.17	0.9 ± 0.1	1	1	0
57	00:03:13.9	−30:03:40.2	3.6	96.08	2.3 ± 0.2	1	1	1
59	00:01:58.5	−30:03:39.1	3.2	61.6	1.6 ± 0.2	3	0	0
61	00:02:22.8	−30:03:23.7	3.6	61.56	4.7 ± 0.5	1	0	0
66	00:02:22.7	−30:02:52.3	2.2	101.53	3.6 ± 0.3	1	1	1
67	00:02:12.2	−30:02:32.2	2.3	85.63	3.3 ± 0.3	1	0	0
70	00:03:39.9	−30:02:13	5.6	65.82	1 ± 0.2	2	1	1
75	00:02:35	−30:01:39.4	5.7	127.78	0.5 ± 0.1	3	1	1
76	00:02:56.7	−30:01:19.4	2.7	135.95	1.2 ± 0.1	3	1	0
77	00:03:29.7	−30:01:18.9	3.1	82.77	4.7 ± 0.3	3	2	2
79	00:03:29.9	−30:01:9	1.9	83.02	0.3 ± 0.1	2	2	2
80	00:03:24.5	−30:01:2.3	3.1	85.73	0.4 ± 0.1	5	1	2
83	00:02:9.4	−30:00:35.9	2.3	83.63	3.7 ± 0.3	2	0	1
85	00:02:50.9	−30:00:20.6	3.6	136.54	0.5 ± 0.1	2	0	0
87	00:01:55.5	−30:00:11.2	4.1	61.7	0.7 ± 0.2	1	0	0
88	00:01:53.9	−29:59:49.1	4.6	54.03	2 ± 0.3	2	1	1
92	00:02:11.4	−29:59:33	3	87.55	1.5 ± 0.2	1	0	0
94	00:02:25.4	−29:59:22.8	5.5	114.85	0.6 ± 0.1	3	2	2
97	00:02:41.7	−29:58:55.8	3.9	138.75	1.3 ± 0.1	1	1	1
98	00:02:45.3	−29:58:50.7	3.7	141.24	1.4 ± 0.1	6	1	1
99	00:01:35.6	−29:58:48.6	5	25.82	3.1 ± 0.6	1	1	1
101	00:03:18.2	−29:58:47.2	1.8	105.95	2.1 ± 0.2	1	1	0
112	00:02:39	−29:57:43.2	5.6	131.12	0.5 ± 0.1	3	0	0
115	00:03:4.6	−29:57:9.6	2.2	121.31	0.9 ± 0.1	1	0	0
116	00:01:54.4	−29:57:8.8	1.7	58.05	0.3 ± 0.1	3	1	1
117	00:03:8.2	−29:57:9.1	4.5	114.78	1 ± 0.2	1	0	0
119	00:02:10	−29:56:48.2	3.3	55.43	0.6 ± 0.2	1	0	0
120	00:03:1.8	−29:56:46.1	2.9	122.38	0.3 ± 0.1	1	0	0
127	00:02:35.1	−29:55:57	1.7	116.24	7.7 ± 0.3	2	0	0
130	00:02:55.9	−29:55:37.8	4.1	120.09	1.4 ± 0.2	6	1	1
131	00:03:11.1	−29:55:20.7	3.1	87.74	1.2 ± 0.2	2	1	1
135	00:02:41.7	−29:55:10.5	4.1	115.99	0.4 ± 0.1	1	0	0
136	00:02:45.2	−29:55:3.6	2.2	117.02	3.2 ± 0.2	4	0	1
138	00:02:30.8	−29:54:48	3.9	103.77	0.5 ± 0.1	1	0	0
139	00:01:49.1	−29:54:47.2	4.1	47.41	3.5 ± 0.4	1	0	0
141	00:02:44.3	−29:54:41.8	2.8	112.57	0.4 ± 0.1	13	2	2
143	00:03:20.9	−29:54:35.7	4.1	84.59	0.6 ± 0.1	1	0	1
144	00:02:8.6	−29:54:32.5	3.5	69.55	1.1 ± 0.2	1	1	1
145	00:03:5.2	−29:54:24.8	1.5	87.17	0.3 ± 0.1	1	0	0

Table A.1. continued.

No. Src X	RA (J2000)	Dec (J2000)	Pos. Err. arcsec	Exp. time ks	Rate cts/ks	No. opt. id. USNO	No. opt. id. GSC2	No. opt. id. 2MASS
146	00:03:2.6	−29:54:23.7	1.8	105.89	7.1 ± 0.3	1	0	0
147	00:02:36.2	−29:54:15.7	4	94.62	0.5 ± 0.1	3	2	2
148	00:01:54	−29:54:5.6	2.9	51.82	2.7 ± 0.3	1	0	0
150	00:03:22.6	−29:53:52.2	2	78.48	6.9 ± 0.4	1	1	1
151	00:02:38.4	−29:53:48	2.5	103.99	2.2 ± 0.2	3	0	0
153	00:02:0.9	−29:53:47.4	4.6	58.74	1.8 ± 0.3	1	0	0
154	00:02:18.8	−29:53:28.4	5.7	79.43	0.8 ± 0.2	3	0	1
155	00:02:41.7	−29:53:0.9	3.6	97.51	0.7 ± 0.1	1	0	0
156	00:03:36.6	−29:52:57	4.4	26.05	1.1 ± 0.3	3	0	0
158	00:02:2.1	−29:52:38.6	2.9	49.35	2.9 ± 0.4	1	1	1
161	00:03:5.6	−29:52:0.4	3	82.74	1.6 ± 0.2	6	1	2
165	00:03:9.3	−29:51:38.7	3.6	77.89	0.9 ± 0.2	3	1	1
166	00:02:59.4	−29:51:32.9	3	71.74	0.6 ± 0.1	1	1	0
169	00:02:23.4	−29:50:40.4	2.6	68.55	3.1 ± 0.3	1	1	1
170	00:02:18.4	−29:50:32.4	4.2	61.95	0.7 ± 0.2	2	0	0
172	00:02:26.7	−29:50:14.6	3.3	68.27	1.3 ± 0.2	1	0	0
174	00:03:0.7	−29:49:44.5	3.3	61.98	5.5 ± 0.5	2	1	1
178	00:02:52.6	−29:49:36.9	5.2	72.69	1.1 ± 0.2	1	1	1
180	00:02:21	−29:49:19.6	3.7	41.42	5.8 ± 0.6	4	0	0
182	00:02:14.6	−29:49:3.5	3.2	20.61	13.8 ± 1.1	4	1	1
185	00:03:3.8	−29:48:19.9	2.5	61.46	1 ± 0.2	1	0	0
186	00:02:35.9	−29:48:14.4	3.6	60.39	4.1 ± 0.4	2	1	1
188	00:02:43.3	−29:47:39.5	3.5	48.31	0.6 ± 0.2	2	0	0
190	00:02:47.9	−29:46:36.9	4.6	23.82	4.1 ± 0.6	3	1	1

References

Anders, E., & Grevesse, N. 1989, Geochim. Cosmochim. Acta, 53, 197

Briggs, K. R., & Pye, J. P. 2003, MNRAS, 345, 714

Cutri, R. M., Skrutskie, M. F., van Dyk, S., et al. 2003, VizieR Online Data Catalog, 2246, 0

Damiani, F., Flaccomio, E., Micela, G., et al. 2003, ApJ, 588, 1009

Damiani, F., Maggio, A., Micela, G., & Sciortino, S. 1997a, ApJ, 483, 350

Damiani, F., Maggio, A., Micela, G., & Sciortino, S. 1997b, ApJ, 483, 370

de Epstein, A. E. A., & Epstein, I. 1985, AJ, 90, 1211

Edvardsson, B., Pettersson, B., Kharrazi, M., & Westerlund, B. 1995, A&A, 293, 75

Epstein, I. 1968, AJ, 73, 556

Feigelson, E. D., & Nelson, P. I. 1985, ApJ, 293, 192

Gagné, M., Caillault, J., & Stauffer, J. R. 1995, ApJ, 450, 217

Ghizzardi, S. 2001, EPIC-MCT-TN-011, Tech. rep., EPIC Milano Calibration Team

Jardine, M. 2004, A&A, 414, L5

Jardine, M., & Unruh, Y. C. 1999, A&A, 346, 883

Jeffries, R. D., & James, D. J. 1999, ApJ, 511, 218

Lang, K. R. 1992, Astrophysical Data I. Planets and Stars (Astrophysical Data I. Planets and Stars, X, 937, 33 Figs. Springer-Verlag Berlin)

Micela, G. 2002, in Stellar Coronae in the Chandra and XMM-NEWTON Era, ASP Conf. Ser., 277, 263

Micela, G., Sciortino, S., Favata, F., Pallavicini, R., & Pye, J. 1999a, A&A, 344, 83

Micela, G., Sciortino, S., Harnden, et al. 1999b, A&A, 341, 751

Micela, G., Sciortino, S., Kashyap, V., Harnden, F. R., & Rosner, R. 1996, ApJS, 102, 75

Monet, D. G., Levine, S. E., Canzian, B., et al. 2003, AJ, 125, 984

Panagi, P. M., & O'Dell, M. A. 1997, A&AS, 121, 213

Pillitteri, I., Micela, G., Sciortino, S., & Favata, F. 2003, A&A, 399, 919

Pizzolato, N., Maggio, A., Micela, G., Sciortino, S., & Ventura, P. 2003, A&A, 397, 147

Pizzolato, N., Ventura, P., D'Antona, F., et al. 2001, A&A, 373, 597

Randich, S. 1997, Memorie della Societa Astronomica Italiana, 68, 971

Randich, S., Schmitt, J. H. M. M., Prosser, C. F., & Stauffer, J. R. 1996, A&A, 305, 785

Robichon, N., Arenou, F., Mermilliod, J., & Turon, C. 1999, A&A, 345, 471

Saxon, R. D. 2002, XMM-CCF-REL-116, Tech. rep., XMM-SOC

Schmitt, J. H. M. M. 1997, A&A, 318, 215

Sciortino, S., Micela, G., Damiani, F., et al. 2001, A&A, 365, L259

Siess, L., Dufour, E., & Forestini, M. 2000, A&A, 358, 593

Smith, R. K., Brickhouse, N. S., Liedahl, D. A., & Raymond, J. C. 2001, ApJ, 556, L91

Stauffer, J. R., Caillault, J.-P., Gagne, M., Prosser, C. F., & Hartmann, L. W. 1994, ApJS, 91, 625

Strüder, L., Briel, U., Dennerl, K., et al. 2001, A&A, 365, L18

Turner, M. J. L., Abbey, A., Arnaud, M., et al. 2001, A&A, 365, L27

Westerlund, B. E., Lundgren, K., Pettersson, B., Garnier, R., & Breysacher, J. 1988, A&AS, 76, 101

Online Material

Appendix A: Unidentified X−ray sources

Table A.1. Table of X-ray unidentified X-ray source positions and properties. The Name column follows the naming convention adopted for the unidentified *XMM* sources. The exposure times and the count rates are scaled to the MOS1 instrument.
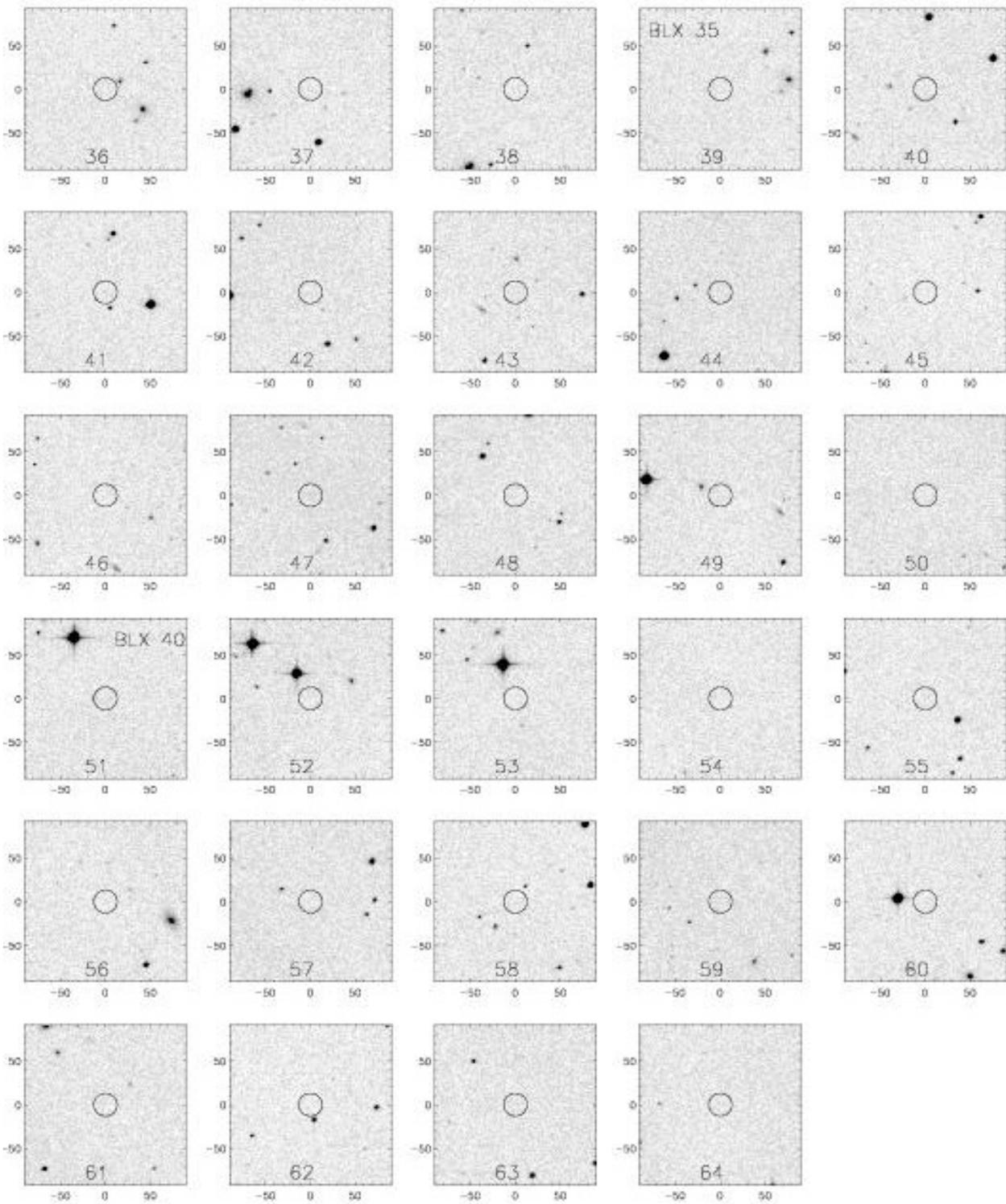
	Name	RA J2000	Dec J2000	Offaxis arcmin	Significance	Time ks	Count rate cts ks^{-1}
1	XMMU J000142.4-295745	00:01:42.4	−29:57:45.7	12.81	6.08	34.22	0.64 ± 0.2
2	XMMU J000145-295441	00:01:45	−29:54:41.5	12.97	25.69	28.67	13.85 ± 1.08
3	XMMU J000146-295946	00:01:46	−29:59:46.7	11.98	6.65	48.05	1.46 ± 0.29
4	XMMU J000155.1-300200	00:01:55.1	−30:02:9.2	10.44	27.82	59.54	7.33 ± 0.5
5	XMMU J000158.2-295511	00:01:58.2	−29:55:11.4	10.12	5.8	59.44	0.56 ± 0.15
6	XMMU J000200.7-295118	00:02:00.7	−29:51:18.3	11.8	17.2	41.55	34.7 ± 5.2
7	XMMU J000200.1-300859	00:02:0.1	−30:08:59.4	13.29	9.21	45.81	1.7 ± 0.33
8	XMMU J000206.3-295820	00:02:6.3	−29:58:20.4	7.61	13.2	77.49	1.52 ± 0.2
9	XMMU J000210.8-295437	00:02:10.8	−29:54:37.7	7.98	7.88	70.62	1.11 ± 0.21
10	XMMU J000213.4-295600	00:02:13.4	−29:56:3.6	6.77	10.08	76.78	1.22 ± 0.2
11	XMMU J000214.2-295924	00:02:14.2	−29:59:24.9	5.87	7.31	50.26	1 ± 0.23
12	XMMU J000216.6-300300	00:02:16.6	−30:03:8.8	6.68	7.48	90.64	0.66 ± 0.13
13	XMMU J000219.3-295155	00:02:19.3	−29:51:55.7	8.63	14.07	71.67	1.6 ± 0.21
14	XMMU J000219.3-300015	00:02:19.3	−30:00:15.7	4.89	8.64	103.13	0.7 ± 0.12
15	XMMU J000219.5-295700	00:02:19.5	−29:57:9.8	5.1	7.26	99.36	0.48 ± 0.11
16	XMMU J000225.4-295614	00:02:25.4	−29:56:14.5	4.49	22.81	102.27	2.43 ± 0.2
17	XMMU J000226.8-300227	00:02:26.8	−30:02:27.2	4.56	8.82	108.62	0.97 ± 0.16
18	XMMU J000232.2-295941	00:02:32.2	−29:59:41.2	2.04	7.91	127.29	0.72 ± 0.13
19	XMMU J000232.5-300317	00:02:32.5	−30:03:17.1	4.57	21.04	114.98	2 ± 0.18
20	XMMU J000236.9-300916	00:02:36.9	−30:9:16.9	10.2	4.97	70.53	0.76 ± 0.19
21	XMMU J000237.3-295845	00:02:37.3	−29:58:45	0.94	4.81	132.34	0.33 ± 0.08
22	XMMU J000238.2-295624	00:02:38.2	−29:56:24.1	2.81	5.51	122.69	0.17 ± 0.05
23	XMMU J000243.8-300711	00:02:43.8	−30:07:11.1	8.07	13.33	92.33	1.99 ± 0.22
24	XMMU J000247-295347	00:02:47	−29:53:47.9	5.47	5.67	105.8	0.29 ± 0.08
25	XMMU J000251.2-300200	00:02:51.2	−30:02:9.1	3.71	5.79	135.26	0.4 ± 0.09
26	XMMU J000251.3-295544	00:02:51.3	−29:55:44	4.04	11.13	115.06	0.89 ± 0.13
27	XMMU J000252.8-295200	00:02:52.8	−29:52:9.4	7.41	9.25	89.78	1.33 ± 0.2
28	XMMU J000252.9-295700	00:02:52.9	−29:57:7.4	3.22	5.44	132.34	0.26 ± 0.07
29	XMMU J000253.7-295948	00:02:53.7	−29:59:48.7	2.78	44.3	141.6	5.21 ± 0.25
30	XMMU J000254-295800	00:02:54	−29:58:8.8	2.92	10.3	136.83	0.74 ± 0.11
31	XMMU J000254.2-300037	00:02:54.2	−30:00:37.5	3.17	17.89	141.05	1.41 ± 0.14
32	XMMU J000255-301200	00:02:55	−30:12:5	13.29	5.48	56.69	0.78 ± 0.2
33	XMMU J000255.4-301234	00:02:55.4	−30:12:34.2	13.78	4.96	53.99	0.31 ± 0.11
34	XMMU J000256.2-294943	00:02:56.2	−29:49:43.7	9.94	5.9	63.3	0.58 ± 0.14
35	XMMU J000256.8-301338	00:02:56.8	−30:13:38.2	14.89	9.92	48.04	1.16 ± 0.22
36	XMMU J000259.2-295514	00:02:59.2	−29:55:14.3	5.5	7.55	115.44	0.42 ± 0.08
37	XMMU J000300.2-295153	00:03:0.2	−29:51:53.2	8.32	8.23	76.24	1.74 ± 0.28
38	XMMU J000301.6-295031	00:03:1.6	−29:50:31	9.68	4.86	68.44	0.5 ± 0.14
39	XMMU J000301.8-295547	00:03:1.8	−29:55:47.7	5.56	15.58	116.67	1.5 ± 0.16
40	XMMU J000303.2-294900	00:03:3.2	−29:49:5.8	11.11	7.91	65.83	1.25 ± 0.24
41	XMMU J000304.1-300300	00:03:4.1	−30:03:8.8	6.36	29.59	119.2	3.65 ± 0.24
42	XMMU J000305.6-295910	00:03:5.6	−29:59:10.4	5.27	9.16	62.55	0.71 ± 0.16
43	XMMU J000306.3-294939	00:03:6.3	−29:49:39.6	10.91	7.7	69.11	1.08 ± 0.21
44	XMMU J000307.8-295800	00:03:7.8	−29:58:3.2	5.85	10.96	120.61	0.94 ± 0.13
45	XMMU J000308.2-300328	00:03:8.2	−30:03:28	7.27	8.61	81.25	0.9 ± 0.17
46	XMMU J000310.1-294837	00:03:10.1	−29:48:37.3	12.22	7.67	60.47	0.81 ± 0.17
47	XMMU J000311.6-300900	00:03:11.6	−30:9:8.4	11.97	10.69	69.61	1.46 ± 0.22
48	XMMU J000313.7-300047	00:03:13.7	−30:00:47.8	7.23	15.26	114.37	1.33 ± 0.16
49	XMMU J000314.3-294940	00:03:14.3	−29:49:40.5	11.86	7.55	63.9	0.84 ± 0.18
50	XMMU J000317.4-300643	00:03:17.4	−30:06:43.5	10.91	10.03	78.87	1.42 ± 0.21

Table A.1. continued.

	Name	RA J2000	Dec J2000	Offaxis arcmin	Significance	Time s	Count rate cts s^{-1}
51	XMMU J000319.1-300219	00:03:19.1	−30:02:19.1	8.78	27.49	98.67	3.6 ± 0.26
52	XMMU J000319.4-294951	00:03:19.4	−29:49:51.5	12.41	9.53	60.79	1.47 ± 0.24
53	XMMU J000320.7-300149	00:03:20.7	−30:01:49.1	8.96	16.56	97.08	2.01 ± 0.21
54	XMMU J000321.1-300651	00:03:21.1	−30:06:51.3	11.57	6.54	74.44	0.56 ± 0.13
55	XMMU J000323.8-300340	00:03:23.8	−30:03:40	10.26	5.64	84.17	0.74 ± 0.17
56	XMMU J000326.2-300827	00:03:26.2	−30:08:27.7	13.47	12.58	57.47	2.63 ± 0.34
57	XMMU J000326.3-300449	00:03:26.3	−30:04:49.9	11.29	25.72	77.5	4.39 ± 0.33
58	XMMU J000330.5-295642	00:03:30.5	−29:56:42.4	10.95	8.84	67.25	1.36 ± 0.23
59	XMMU J000336.7-295200	00:03:36.7	−29:52:3.8	13.94	5.32	23.17	1.07 ± 0.31
60	XMMU J000337.4-300213	00:03:37.4	−30:02:13.1	12.55	7.66	70.42	0.56 ± 0.12
61	XMMU J000339.1-300842	00:03:39.1	−30:08:42.4	15.76	6.6	34.4	1.81 ± 0.41
62	XMMU J000340.2-295827	00:03:40.2	−29:58:27.7	12.78	4.84	68.39	0.41 ± 0.12
63	XMMU J000341.3-295725	00:03:41.3	−29:57:25.6	13.11	14.14	27.3	4.26 ± 0.54
64	XMMU J000344.2-300034	00:03:44.2	−30:00:34.1	13.7	8.24	57.76	1.74 ± 0.29
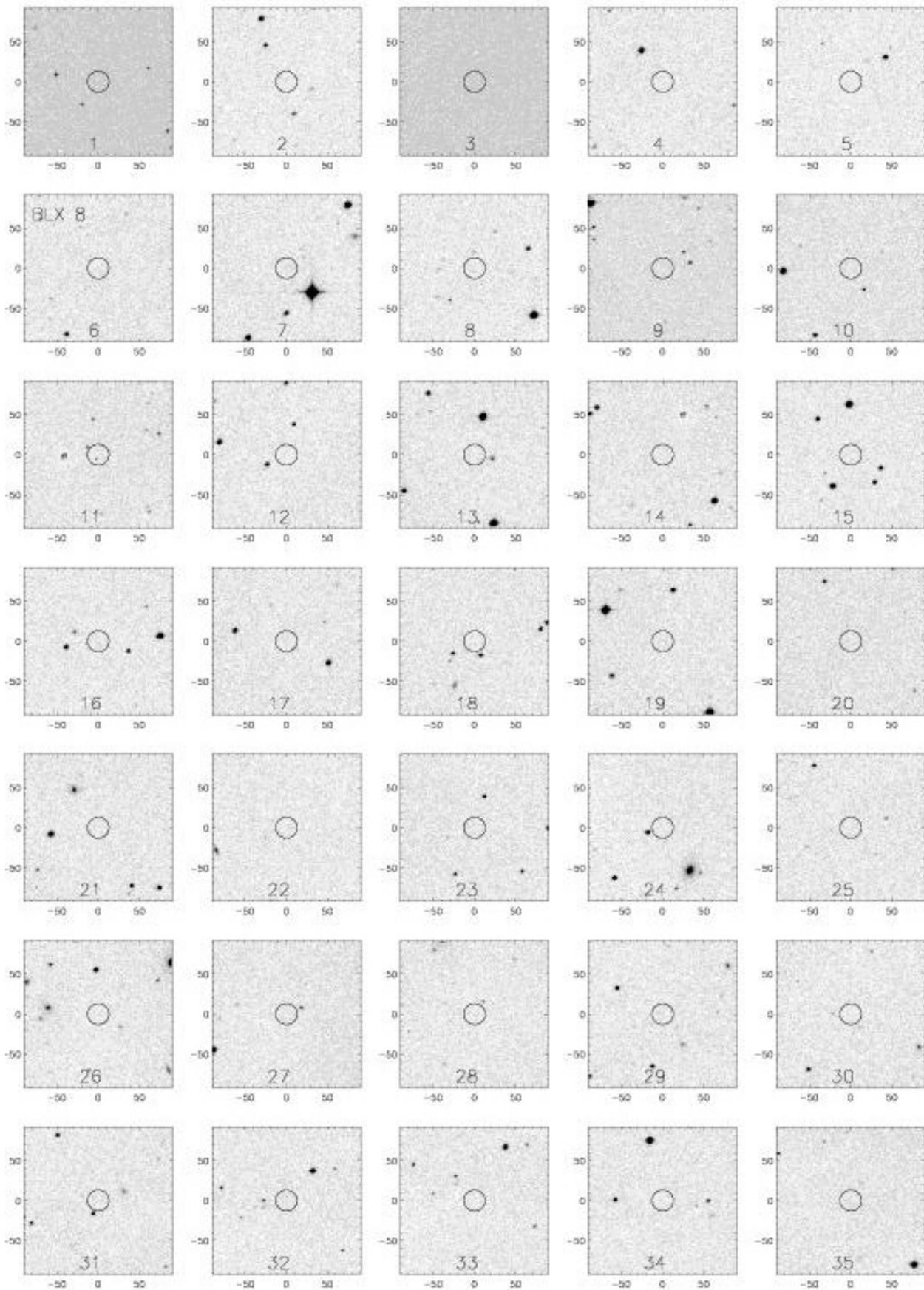
Fig. A.1. DSS2 – IR finding charts (panel widths: 3′ by 3′) centered on X-ray positions of unidentified sources, with Table B.1 numbers indicated at bottom edge of each panel; 13″-radius circles indicate the X-ray/optical matching criterion.

Fig. A.2. As in Fig. A.1.